THE JOURNAL OF PHYSICAL CHEMISTRY C

pubs.acs.org/JPCC Article

Interpretation of Resistance, Capacitance, Defect Density, and Activation Energy Levels in Single-Crystalline $MAPbI_3$

Abul Kalam, Rashmi Runjhun, Apurba Mahapatra, Mohammad Mahdi Tavakoli, Suverna Trivedi, Hadi Tavakoli Dastjerdi, Pawan Kumar, Janusz Lewiński, Manoj Pandey, Daniel Prochowicz,* and Pankaj Yadav*

Cite This: J. Phys. Chem. C 2020, 124, 3496−3502

ABSTRACT: Hybrid inorganic−organic lead halide perovskites have attracted a significant research interest in the last 10 years due to their broad-area applications in optoelectronic devices such as solar cells, lasers, photodetectors, and light-emitting diodes (LEDs). Fundamental understanding of the charge transportation, defect density, and activation energy is very important for the further progress of this class of semiconductors. Here, we shed light on the interpretation of resistance, capacitance, defect density, and activation energy levels in single-crystalline methylammonium lead iodide ($MAPbI_3$). In particular, the impedance response of the $MAPbI_3$ crystal as a function of applied bias and temperature (under both increasing and decreasing temperature cycles) is studied for the first time. From the detailed bias- and temperature-dependent studies, we found that the low-frequency capacitance values are influenced by ion density and mobility. Consequently, single-crystalline $MAPbI_3$ depicts an activation energy of 0.53−0.54 eV with an exceptionally low electronic trap density of 0.96×10^{10} cm^{-3}. The present study illustrates that the net electrochemical impedance spectra are due to ionic capacitance coupled to a resistance. The associated resistance is related to the conductivity of the perovskite crystal. These findings are helpful to understand the fundamental electrical properties of the $MAPbI_3$ single crystal, which could be useful for the further advancement of perovskite single-crystal-based applications.

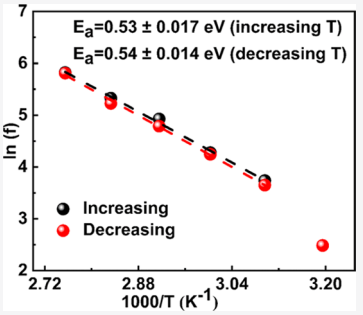

1. INTRODUCTION

In the last 10 years, hybrid inorganic−organic lead halide perovskites have become the center of research interest as one of the most promising candidates for the development of next-generation photovoltaic[1−4] and optoelectronic devices.[5−7] These semiconductors exhibit outstanding electrical and optical properties with the scopes of cost-effectiveness and ease of thin-film fabrication processing.[8,9] However, low operational stability[10] and polarization at low frequencies/long time scales affect the charge transport and recombination during the operation of devices.[11,12] It has been reported that issues mainly governed by ions and vacancy conductions need to be addressed to make perovskite solar cells (PSCs) commercially available.[13,14]

Recently, extensive efforts have been devoted to study the growth methods and physicochemical characterizations of single-crystalline metal halide perovskites.[15] Methylammonium lead iodide ($MAPbI_3$) is a prototypical photoabsorber in PSCs,[16,17] and its single-crystalline form exhibits higher carrier diffusion length and carrier lifetime and a lower trap state density than the corresponding polycrystalline perovskite films.[18,19] A number of studies involving other metal halide perovskites have also univocally shown that the optoelectronic properties of the single-crystalline perovskites are much better compared to those of pellets or thin-film counterparts due to the less amount of grain boundaries and defects.[18,20−22] Therefore, the utilization of perovskite single crystals for optoelectronic application has emerged as a new direction for boosting the efficiency and moisture stability of PSCs.[23−25]

It is well established that migration of ionic species in a perovskite leads to instability in PSCs and has also been proposed as a possible cause of the hysteresis effect.[26] The activation energy of migrating ions in $MAPbI_3$ has been estimated theoretically and experimentally and covered a wide range of 0.2−0.6 eV.[20,26−33] Due to this discrepancy on the energy barrier that determines the ion transport, it is still desirable to shed more light on the mechanism of ion conduction in perovskite materials.[34] The activation energy and electronic defect density of perovskite single crystals found in the literature are summarized in Table 1.

In this work, we report on the bias- and temperature-dependent behavior of single-crystalline $MAPbI_3$ using electrochemical impedance spectroscopy (EIS) and capacitance spectroscopy. Our results reveal that the low-frequency

Received: December 6, 2019
Revised: January 17, 2020
Published: January 20, 2020

https://dx.doi.org/10.1021/acs.jpcc.9b11343
J. Phys. Chem. C 2020, 124, 3496−3502

Table 1. Calculated Values of Activation Energy and Electronic Defect Density for Perovskite Single Crystals

activation energy and trap density of $MAPbI_3$ single crystals		
activation energy	measurements	refs
0.624 eV (I^-) (single crystal)	temperature-dependent ion conductivity	29
0.45 eV (I^-) 0.70 eV (MA^+) (single crystal)	polarization-induced current−voltage hysteresis	30
0.58 eV (I^-)	first principles	28
2.31 eV (Pb^{2+})		
0.84 eV (MA^+)		
0.82 eV (thin film)	temperature-dependent ion conductivity	31
0.119 eV (MA^+)	Quasi-elastic neutron scattering measurements and first-principles analysis	32
0.53 eV (I^-)	temperature-dependent electrochemical impedance spectroscopy (EIS)	26
0.51 eV (I^-)	temperature-dependent ion conductivity from Warburg impedance	26
1.05 eV (single crystal)	temperature-dependent ion conductivity	27
0.5 eV (thin film)		
0.1 (I^-)	NMR spectra	20
0.43 eV (I^-) (pellets)	temperature-dependent ion conductivity	33
trap density of $MAPbX_3$ (X = I, Br, Cl) single crystal using space-charge-limited current (SCLC) regime		
single crystals	**trap density (cm^{-3})**	**refs**
$MAPbI_3$	5.8×10^9	35
$MAPbI_3$	3.3×10^{10}	18
$MAPbCl_3$	3.1×10^{10}	33
$MAPbI_3$	1.4×10^{10}	19
$MAPbBr_3$	3×10^{10}	19

capacitances are influenced by the ion density and mobility. We demonstrate that the electrical parameters such as capacitance, resonance time, and impedance are temperature- and voltage-dependent. Understanding the behavior of these parameters can provide a way to design and optimize perovskite crystals employed for various optoelectronic applications. In this regard, the conventional electrical direct current (DC) measurements still remain limited. The activation energy corresponding to ion migration was calculated to be in the range of 0.53−0.54 eV. Moreover, we find that the $MAPbI_3$ crystal depicts an exceptionally low trap density of 0.96×10^{10} cm^{-3}. This study also shows that the EIS response of the $MAPbI_3$ single crystal exhibits different behavior from that observed in PSCs. While the EIS spectra of PSCs are defined by two semicircles, a single semicircle is observed for perovskite single crystal. The present study illustrates that the net electrochemical impedance spectra are due to ionic capacitance coupled to a resistance. The associated resistance is related to the conductivity of the perovskite crystal. These results are helpful to understand the fundamental electrical properties of single-crystalline $MAPbI_3$, which could be useful for the further advancement of perovskite single-crystal-based applications.

2. EXPERIMENTAL SECTION

2.1. Synthesis of $MAPbI_3$ Single Crystals. The perovskite crystals were grown briefly using a 1.0 M $MAPbI_3$ solution prepared by dissolving equimolar amounts of precursors in γ-butyrolactone at 60 °C overnight. Before crystallization, the solution was filtered using a 0.2 μm pore size PTFE filter. Next, 2 mL of the filtered precursor solution was kept at 160 °C for 30 min in an oil bath, which resulted in the growth of very small seed crystals. The seed crystal solution was further heated at 120 °C for 3 h. Finally, the remaining solution was discarded and the crystals were washed with acetone 2−3 times and then dried.

2.2. Characterization of Perovskite Single Crystals. Temperature-dependent powder X-ray diffraction (XRD) patterns were recorded with an Empyrean diffractometer (PANalytical) equipped with a copper lamp (40 kV, 40 mA). The samples were mounted inside the Anton Paar TTK-450 sample chamber for nonambient X-ray diffraction experiments. For the measurements, Ni-filtered Cu Kα (λ = 0.154 nm) radiation was used and was detected with an X'Celerator 1D detector in the Bragg−Brentano θ−θ geometry. The XRD patterns were recorded over a 2θ range of 10−50° without rotating the sample. EIS measurements were performed using a potentiostat Autolab equipped with a frequency response analyzer. EIS measurements were performed as a function of applied bias and temperature.

3. RESULTS AND DISCUSSION

3.1. Effect of the Applied Bias. $MAPbI_3$ single crystals were grown using a recently reported procedure (for details, see the Section 2).[36] The electrical properties of a $MAPbI_3$ single crystal were studied using alternating current (AC) impedance spectroscopy in the frequency range of 1 Hz to 1 MHz under the dark condition in the temperature range of 30−90 °C. Additionally, a variable direct current (DC) voltage is applied on the sample during the electrochemical impedance spectroscopy (EIS) measurement. The impedance curves of the $MAPbI_3$ single crystal are found to be strongly affected by the measurement conditions. To perform temperature- and bias-dependent EIS measurements, thin layers of silver (Ag) were deposited on both sides of a $MAPbI_3$ single crystal with

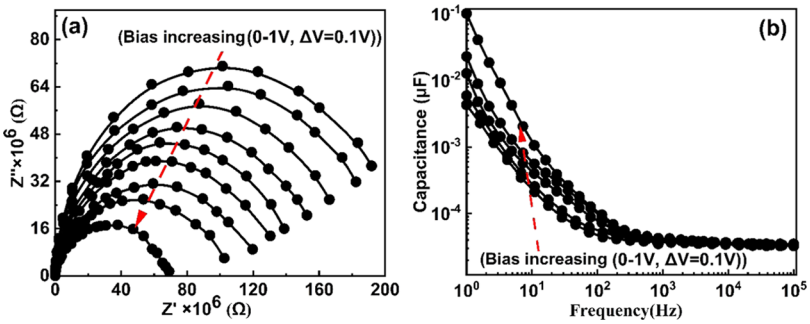

Figure 1. EIS data of $MAPbI_3$ single crystal at ambient temperature (303 K) as (a) a function of applied bias measured under the dark condition and (b) capacitance $\left(\frac{\mathrm{Im}(1/Z)}{\omega}\right)$ plot as a function of applied bias in the frequency range of 1 MHz to 1 Hz.

https://dx.doi.org/10.1021/acs.jpcc.9b11343
J. Phys. Chem. C 2020, 124, 3496−3502

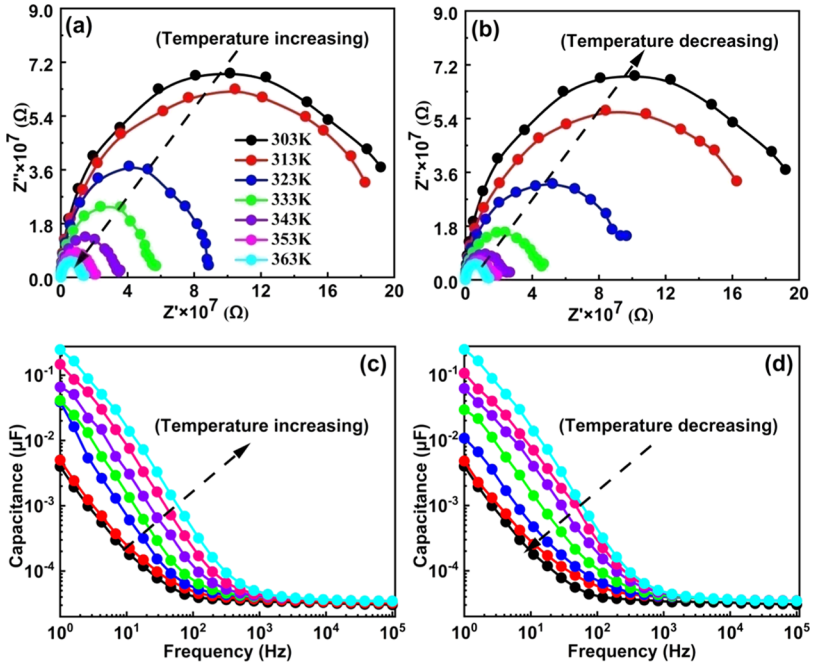

Figure 2. Dark EIS measurement of the $MAPbI_3$ single crystal at 0 V DC bias in the frequency range of 1 MHz to 1 Hz as a function of temperature (313−363 K). Nyquist plots of the crystal (indicating approximately semicircles), by (a) increasing and (b) decreasing temperature. Apparent capacitance $\left(\frac{\mathrm{Im}(1/Z)}{\omega}\right)$ of the crystal vs frequency curves, by (c) increasing and (d) decreasing temperature (the value of capacitance is increased with increasing temperature in the low-frequency region <1000 Hz).

dimensions of $2.26 \times 2.07 \times 0.6$ mm^3. To confirm the validity of results, we repeated each measurement several times under the same conditions. All experiments were conducted on different crystals from the same batch. We observed that the crystals have different sizes even when crystallized from the same batch. Therefore, in all further experiments, we use the measuring units without any conversion factor.

First, we conduct the EIS measurement as a function of applied DC bias at ambient temperature, as shown in Figure 1a. The Nyquist plots of $MAPbI_3$ crystals show a suppressed single semicircle. The distortion in the semicircle is due to the involvement of the physical process associated closely with the low and high frequencies. To test the reproducibility of our results, we measured the EIS response of other $MAPbI_3$ crystals and found similar behavior (see Figure S1). A decrease in the radii of the semicircles was observed with an increase in the applied bias from 0 to 1 V, which suggests that the applied potential has a significant impact on the charge characteristics.[26] In our previous works, we demonstrated that the EIS spectra (Nyquist plots) of PSCs show two well-separated semicircles in the dark and under illumination.[37,38] These semicircles were associated with the low- and high-frequency responses of the devices. The high-frequency response is due to the recombination resistance and geometrical capacitance, whereas the low-frequency response is due to the coupled response of ions and charges.[39] In the present case, we believe that the single semicircle is due to symmetrical contacts and the single-crystal nature of $MAPbI_3$. In PSCs, the recombination takes place at interfaces between the perovskite absorber layer and contacts and at grain boundaries. In EIS, these features are observed in the high-frequency region (10^5−10^6 Hz) and analyzed by the real part of high-frequency impedance.[37,38,40] However, no such response is observed for $MAPbI_3$ single crystals. It is possible that the absence of grain boundaries, use of symmetrical contacts, and dominant ionic response in the low-frequency capacitance (<10^3 Hz) have suppressed the high-frequency features of $MAPbI_3$ crystals. To further test the occurrence of Nyquist spectra with a central frequency in the range of <10^3 Hz, $MAPbBr_3$ single crystals were synthesized and measured. Figure S2 shows the single semicircle Nyquist spectra for the $MAPbBr_3$ crystal, confirming that the EIS spectra of the single crystal differ from those found in PSCs. Figure S3 shows the resonance time constant (τ) as a function of applied bias. The resonance time (τ) is obtained using the expression $\tau = 1/\omega_{(\mathrm{min})}$, where $_{(\mathrm{min})}$ is the angular frequency, corresponding to the minimum of imaginary of complex impedance. We found that τ is affected by the applied bias. Note that the obtained magnitude of τ in the range of ms is too high in magnitude to explain the electronic charge recombination, which generally occurs in the time scale of μs. The origin of the τ in $MAPbI_3$ single crystals is another topic, which requires further discussion.

Figure 1b shows the capacitance vs frequency (C−F) plots as a function of applied bias. Two distinguishing features of capacitance corresponding to low- and high-frequency regions are observed. In general, the capacitance at low frequency (<10^3 Hz) is associated with ion and charge accumulation or electrode polarization, whereas the high-frequency capacitance is due to geometrical capacitance.[41] With the increase in the applied bias, the low-frequency capacitance increases and also shifts to high frequency. Neukom et al. analytically and experimentally investigated the role of ion density and mobility in the C−F plot of perovskites.[42] It was concluded that a variation in the ion mobility changes the transition frequency; the low-frequency capacitance value increased with increasing ion density. Another study revealed that a higher bulk conductivity leads to a higher capacitance, which further increases with the applied bias and illumination.[43] Therefore, the obtained capacitance response at

https://dx.doi.org/10.1021/acs.jpcc.9b11343
J. Phys. Chem. C 2020, 124, 3496−3502

the frequency (<10^3 Hz) of $MAPbI_3$ crystals is said to be influenced by the ion density and mobility.

To further investigate the change in the conductivity of $MAPbI_3$ crystals due to the applied bias, the value of resistance as a function of applied bias is plotted (Figure S4). The value of resistance was obtained from the real part of the impedance spectra. We observe a gradual decrease in resistance with increasing bias. This phenomenon is consistent with the recent study by Moia et al., in which this behavior was described as the "ionic-to-current amplification", and mobile ions open the door for the electronic charge transport.[43] Figure S5a shows the current−voltage ($I-V$) characteristic of the $MAPbI_3$ crystal measured under forward and reverse directions and the dark condition at a scan rate of 100 mV s^{-1}. The measured $I-V$ response exhibits the hysteresis feature. In perovskite solar cells, the existence of hysteresis is very common and generally assigned to the ionic nature of the perovskite semiconductor. The difference in the current magnitude during $I-V$ measurements in forward and reverse directions (see Figure S5a) confirms that the net electronic current is influenced by the ions. Figure S5b shows the $I-V$ plot of the $MAPbI_3$ crystal as a function of the voltage sweep rate. It was found that iodine ions are responsible for hysteresis in PSCs due to its 4 orders higher diffusion coefficient (10^{-12} cm^2 s^{-1}) compared to MA^+ ions (10^{-16} cm^2 s^{-1}).[28,44] In the present case, the increase in hysteresis is observed at a low scan rate. At a low scan rate, the iodine ions have sufficient time to move through the perovskite structure. Moreover, it is well established that the hysteresis index is proportional to the magnitude of low-frequency capacitance.[45,46] From the observation of $C-F$ and $I-V$ analyses, we conclude that the low-frequency capacitance and hysteresis in the $I-V$ curve are due to mobile ions.

3.2. Effect of Applied Temperature at Fixed Bias. To study the effect of temperature on the EIS response of the $MAPbI_3$ crystal, the EIS spectra were collected at a range of different temperatures (303−363 K) at 0 V bias under the dark condition. Before the measurement, powder X-ray diffraction of the $MAPbI_3$ crystal was measured to ensure the structural stability at applied temperatures. The temperature-dependent powder X-ray diffraction (pXRD) analysis confirms the structural stability of the $MAPbI_3$ crystal after heating up to 90 °C (Figure S6). Moreover, we observed the tetragonal−cubic phase transition between 323 and 333 K.[47]

The impedance responses in the form of Nyquist and $C-F$ plots as a function of temperature are shown in Figure 2. The collected Nyquist plots exhibit a similar trend upon increasing and decreasing temperatures, which indicates that the electronic properties of the investigated crystal are stable under probed temperature ranges. We observe a decrease in the semicircle radius of the EIS spectra with increasing temperature (Figure 2a). Moreover, after plotting the Bode curves shown in Figure S7, there is a shift in resonance frequency toward the higher-frequency range with increasing temperature. The observed shift suggests that there is a temperature-activated process. Comparing our results with other reported works on EIS studies of PSCs under different temperatures, the following key observations are concluded:

1. In PSCs, the high-frequency resonance peak is generally observed in the frequency range of 10^5-10^6 Hz and mainly assigned to the recombination resistance and geometrical capacitance.[38,40] In the present study on the $MAPbI_3$ crystal, the frequency resonance peak was observed in the range of 10^2-10^3 Hz and there is no peak in the frequency range of 10^5-10^6 Hz.
2. According to the recent report by García-Rodríguez et al. on the role of bromide content in iodine migration, the temperature has a least impact on the high-frequency spectra (10^5-10^6 Hz).[40] In turn, the maximum shift at low- and mid-frequency (10^2-10^3 Hz) spectra is observed with change in temperature. Consistent with the finding of the mid-frequency (10^2-10^3 Hz) spectra of PSCs, the $MAPbI_3$ crystal also shows a similar temperature-dependent behavior in the same frequency range. The shift in the probed frequency range is seen by plotting the variation of τ against temperature, as shown in Figure S8.

These results suggest that the EIS response of PSCs is different from that found in single crystals, where the net capacitance response in the frequency range (<10^3 Hz) is mainly governed by the mobile ions in the later case. Note that parameters such as capacitance, resonance time, and impedance are found to be temperature- and voltage-dependent. Understanding the effect of these parameters can provide a way to design and optimize perovskite crystals, which are employed for various optoelectronic applications, while the conventional electrical DC measurements, which are mainly employed for electrical measurements, remain limited in this regard. After establishing the fact that the EIS response of crystals is due to ionic capacitance coupled to a resistance, in the next step, we calculate the activation energy of ions and electronic density of defects.

Figure 2c,d shows the frequency-dependent capacitance plots at different temperatures. No significant difference is observed between the $C-F$ curves measured upon increasing and decreasing temperature cycles. As expected, the capacitance in the low-frequency region increases with increasing temperature. From the obtained $C-F$ plot, a change in inflection frequencies (f_0) in the range of 10^1-10^2 Hz is observed. Figure 3 shows the plots of $\ln(f_0)$ vs $1/T$. By taking the slope of these curves, activation energies of 0.53 ± 0.17 and 0.54 ±0.14 eV during heating and cooling of the $MAPbI_3$ crystal were obtained, respectively. A small difference in the value of activation energy for the $MAPbI_3$ crystal was observed during the heating and cooling measurement. This might be due to the local lattice distortion connected with the tetragonal−cubic phase transition. In the literature, point defects due to the ion migration in $MAPbI_3$ have been related to the activation energy ranging from 0.1 to 0.6 eV, which depends on the applied characterization method and material crystallinity (Table 1).[26,28,48,49] The

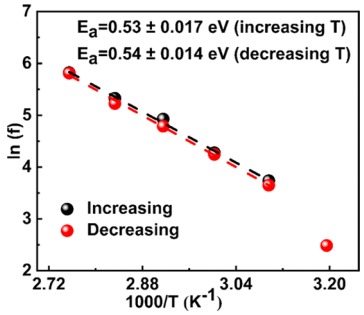

Figure 3. Arrhenius plots of the inflection frequencies vs 1000/T (ln (f_0) vs 1000/T) during increasing and decreasing the temperature of the $MAPbI_3$ single crystal. E_{act} is the activation energy for the traps.

https://dx.doi.org/10.1021/acs.jpcc.9b11343
J. Phys. Chem. C 2020, 124, 3496−3502

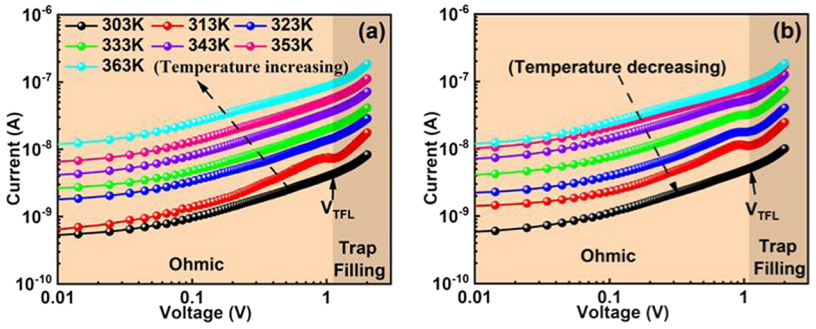

Figure 4. Trap density measurement for the $MAPbI_3$ single crystal. Temperature-dependant dark current−voltage responses of the crystal by (a) increasing and (b) decreasing the temperature.

obtained activation energy corresponds to the ion migration, which further confirms our results that the associated capacitance in the low-frequency range ($<10^3$ Hz) is due to mobile ions. Very recently, Almora et al. have studied the temperature-activated low-frequency capacitance ($<10^1$ Hz) for PSCs and attained $\sim 10^{21}$ eV^{-1} cm^{-3} density of states (DOS).[50] It was stressed that such a high value of DOS is hardly connected to ionic or electronic defects levels.

To calculate the electronic trap states in the crystals, a well-established space-charge-limited current (SCLC) for perovskite crystals is used.[18,19,22,35] To quantify the electronic defect density in $MAPbI_3$ crystals, dark current−voltage (I−V) measurements as a function of temperature were carried out. As shown in Figure 4, the I−V characteristic of the crystal exhibits different slopes at different bias. In the low applied bias, a linear region is observed that causes a sharp rise ($I \alpha V^{n>3}$) at a high applied bias. This voltage is called the kink point or trap-filled limit voltage (V_{TFL}).[51] By considering a linear dependence between trap density (η_{traps}) and V_{TFL}, the defect density is calculated using the given expression

$$\eta_{traps} = \frac{2\varepsilon\varepsilon_0 V_{TFL}}{eL^2} \quad (1)$$

where e and ε_0 are the elementary charge (1.6×10^{-19} C) and vacuum permittivity (8.854×10^{-12} F m^{-1}), respectively, and L and ε are the thickness of the crystal (~0.6 mm) and dielectric constant (28.8)[52] of the $MAPbI_3$ single crystal, respectively. We calculated V_{TFL} for each cycle and estimated the trap density. The average value of η_{traps} equals 0.96×10^{10} cm^{-3}, which is in agreement with the previous study.[18] Interestingly, the trap density is significantly lower than that found in the well-known inorganic semiconductor like single crystals of CIGS,[53] CdTe,[54] or Si.[55] It should be noted here that the applied method is mainly associated with the electronic defect level. To elucidate the role of ions in the electronic trap states, we measure the I−V hysteresis and calculate the trap density (see Figure S5c). From the obtained plot, hysteresis behavior confirms that the change in current is due to ions and has a negligible effect on the trap density. This signature requires further electrical or optical characterization to clearly elucidate the role of ions on trap defect density. Our results confirm that the $MAPbI_3$ single crystal has a very high quality with very low defect density, which is required for high-performance photoelectronic devices such as the photodetector.

4. CONCLUSIONS

In conclusion, we systematically studied the electrical properties of single-crystalline $MAPbI_3$, such as resistance, capacitance, defect density, and activation energy levels. Detailed bias- and temperature-dependent studies revealed that the low-frequency capacitance values are influenced by the ion density and mobility. We found that electrical parameters such as capacitance, resonance time, and impedance are temperature- and voltage-dependent. The calculated activation energy values in the range of 0.53−0.54 eV correspond to ion migration. The $MAPbI_3$ crystal depicts an exceptionally low electronic trap density of 0.96×10^{10} cm^{-3}. These findings are helpful to understand the fundamental electrical properties of single-crystalline $MAPbI_3$.

■ ASSOCIATED CONTENT

Supporting Information

The Supporting Information is available free of charge at https://pubs.acs.org/doi/10.1021/acs.jpcc.9b11343.

Nyquist plots of a $MAPbI_3$ and $MAPbBr_3$ single crystals; relaxation time constant; real impedance; I−V curves under forward and reverse bias; temperature-dependent powder X-ray diffraction (pXRD); phase−frequency Bode plot; and Arrhenius plots of time constant vs $1000/T$ of $MAPbI_3$ single crystal (PDF)

■ AUTHOR INFORMATION

Corresponding Authors

Daniel Prochowicz − *Institute of Physical Chemistry, Polish Academy of Sciences, Warsaw 01-224, Poland;* orcid.org/0000-0002-5003-5637; Email: dprochowicz@ichf.edu.pl

Pankaj Yadav − *Department of Solar Energy, School of Technology, Pandit Deendayal Petroleum University, Gandhinagar 382 007, Gujarat, India*; Email: Pankaj.yadav@sse.pdpu.ac.in, pankajphd11@gmail.com

Authors

Abul Kalam − *Department of Chemistry, Faculty of Science and Research Centre for Advanced Materials Science (RCAMS), King Khalid University, Abha 61413, Saudi Arabia*

Rashmi Runjhun − *Institute of Physical Chemistry, Polish Academy of Sciences, Warsaw 01-224, Poland*

Apurba Mahapatra − *Department of Physics & Astronomy, National Institute of Technology, Rourkela 769008, India*

Mohammad Mahdi Tavakoli − *Department of Electrical Engineering and Computer Science, Massachusetts Institute of Technology, Cambridge, Massachusetts 02139, United States; Department of Materials Science and Engineering, Sharif University of Technology, Tehran 14588, Iran;* orcid.org/0000-0002-8393-6028

https://dx.doi.org/10.1021/acs.jpcc.9b11343
J. Phys. Chem. C 2020, 124, 3496−3502

Suverna Trivedi − *Department of Chemical Engineering, School of Technology, Pandit Deendayal Petroleum University, Gandhinagar 382 007, Gujarat, India*

Hadi Tavakoli Dastjerdi − *Department of Materials Science and Engineering, Massachusetts Institute of Technology, Cambridge, Massachusetts 02139, United States;* orcid.org/0000-0002-8925-5493

Pawan Kumar − *Department of Physics & Astronomy, National Institute of Technology, Rourkela 769008, India*

Janusz Lewiński − *Institute of Physical Chemistry, Polish Academy of Sciences, Warsaw 01-224, Poland; Faculty of Chemistry, Warsaw University of Technology, Warsaw 00-664, Poland;* orcid.org/0000-0002-3407-0395

Manoj Pandey − *Department of Science, School of Technology, Pandit Deendayal Petroleum University, Gandhinagar 382 007, Gujarat, India*

Complete contact information is available at: https://pubs.acs.org/10.1021/acs.jpcc.9b11343

Notes

The authors declare no competing financial interest.

■ ACKNOWLEDGMENTS

A.K. is thankful to Dean of Scientific Research, King Khalid University, for financial support by grant number RGP 2/36/40. R.R. thanks funding from the European Union's Horizon 2020 research and innovation program under the Marie Sklodowska Curie grant agreement no. 711859 and Polish Ministry of Science and Higher Education from the co-funded project, grant agreement no. 3549/H2020/COFUND2016/2. D.P. acknowledges financial support from the HOMING programme of the Foundation for Polish Science co-financed by the European Union under the European Regional Development Fund (POIR.04.04.00-00-5EE7/18-00). P.Y. acknowledges the ORSP of Pandit Deendayal Petroleum University for financial support. PY acknowleges the DST SERB (CRG/2018/000714 and DST Nano Mission (DST/NM/NT/2018/174).

■ REFERENCES

(1) Nie, W.; Tsai, H.; Asadpour, R.; Blancon, J.-C.; Neukirch, A. J.; Gupta, G.; Crochet, J. J.; Chhowalla, M.; Tretiak, S.; Alam, M. A.; et al. High-Efficiency Solution-Processed Perovskite Solar Cells with Millimeter-Scale Grains. *Science* **2015**, *347*, 522−525.

(2) Tavakoli, M. M.; Saliba, M.; Yadav, P.; Holzhey, P.; Hagfeldt, A.; Zakeeruddin, S. M.; Grätzel, M. Synergistic Crystal and Interface Engineering for Efficient and Stable Perovskite Photovoltaics. *Adv. Energy Mater.* **2019**, *9*, No. 1802646.

(3) Park, N.-G. Organometal Perovskite Light Absorbers Toward a 20% Efficiency Low-Cost Solid-State Mesoscopic Solar Cell. *J. Phys. Chem. Lett.* **2013**, *4*, 2423−2429.

(4) Jiang, Q.; Zhao, Y.; Zhang, X.; Yang, X.; Chen, Y.; Chu, Z.; Ye, Q.; Li, X.; Yin, Z.; You, J. Surface Passivation of Perovskite Film for Efficient Solar Cells. *Nat. Photonics* **2019**, *13*, 460−466.

(5) Tavakoli, M. M.; Yadav, P.; Prochowicz, D.; Sponseller, M.; Osherov, A.; Bulović, V.; Kong, J. Controllable Perovskite Crystallization via Antisolvent Technique Using Chloride Additives for Highly Efficient Planar Perovskite Solar Cells. *Adv. Energy Mater.* **2019**, *9*, No. 1803587.

(6) Prochowicz, D.; Runjhun, R.; Tavakoli, M. M.; Yadav, P.; Saski, M.; Alanazi, A. Q.; Kubicki, D. J.; Kaszkur, Z.; Zakeeruddin, S. M.; Lewin'ski, J.; Grätzel, M. Engineering of Perovskite Materials Based on Formamidinium and Cesium Hybridization for High-Efficiency Solar Cells. *Chem. Mater.* **2019**, *31*, 1620−1627.

(7) Tavakoli, M. M.; Tavakoli, R.; Yadav, P.; Kong, J. A Graphene/ZnO Electron Transfer Layer Together with Perovskite Passivation Enables Highly Efficient and Stable Perovskite Solar Cells. *J. Mater. Chem. A* **2019**, *7*, 679−686.

(8) Mahapatra, A.; Prochowicz, D.; Tavakoli, M. M.; Trivedi, S.; Kumar, P.; Yadav, P. A Review on the Aspects of Additive Engineering in Perovskite Solar Cells. *J. Mater. Chem. A* **2020**, *8*, 27−54.

(9) Tavakoli, M. M.; Waleed, A.; Gu, L.; Zhang, D.; Tavakoli, R.; Lei, B.; Su, W.; Fang, F.; Fan, Z. A Non-Catalytic Vapor Growth Regime for Organohalide Perovskite Nanowires Using Anodic Aluminum Oxide Templates. *Nanoscale* **2017**, *9*, 5828−5834.

(10) Berhe, T. A.; Su, W.-N.; Chen, C.-H.; Pan, C.-J.; Cheng, J.-H.; Chen, H.-M.; Tsai, M.-C.; Chen, L.-Y.; Dubale, A. A.; Hwang, B.-J. Organometal Halide Perovskite Solar Cells: Degradation and Stability. *Energy Environ. Sci.* **2016**, *9*, 323−356.

(11) Juarez-Perez, E. J.; Sanchez, R. S.; Badia, L.; Garcia-Belmonte, G.; Kang, Y. S.; Mora-Sero, I.; Bisquert, J. Photoinduced Giant Dielectric Constant in Lead Halide Perovskite Solar Cells. *J. Phys. Chem. Lett.* **2014**, *5*, 2390−2394.

(12) Xiao, Z.; Yuan, Y.; Shao, Y.; Wang, Q.; Dong, Q.; Bi, C.; Sharma, P.; Gruverman, A.; Huang, J. Giant Switchable Photovoltaic Effect in Organometal Trihalide Perovskite Devices. *Nat. Mater.* **2015**, *14*, 193−198.

(13) Tavakoli, M. M.; Dastjerdi, H. T.; Prochowicz, D.; Yadav, P.; Tavakoli, R.; Saliba, M.; Fan, Z. Highly Efficient and Stable Inverted Perovskite Solar Cells Using Down-Shifting Quantum Dots as a Light Management Layer and Moisture-Assisted Film Growth. *J. Mater. Chem. A* **2019**, *7*, 14753−14760.

(14) Bag, M.; Renna, L. A.; Adhikari, R. Y.; Karak, S.; Liu, F.; Lahti, P. M.; Russell, T. P.; Tuominen, M. T.; Venkataraman, D. Kinetics of Ion Transport in Perovskite Active Layers and Its Implications for Active Layer Stability. *J. Am. Chem. Soc.* **2015**, *137*, 13130−13137.

(15) Liu, Y.; Yang, Z.; Liu, S. F. Recent Progress in Single-Crystalline Perovskite Research Including Crystal Preparation, Property Evaluation, and Applications. *Adv. Sci.* **2018**, *5*, No. 1700471.

(16) Prochowicz, D.; Franckevičius, M.; Cieślak, A. M.; Zakeeruddin, S. M.; Grätzel, M.; Lewiński, J. Mechanosynthesis of the Hybrid Perovskite $CH_3NH_3PbI_3$: Characterization and the Corresponding Solar Cell Efficiency. *J. Mater. Chem. A* **2015**, *3*, 20772−20777.

(17) Kojima, A.; Teshima, K.; Shirai, Y.; Miyasaka, T. Organometal Halide Perovskites as Visible-Light Sensitizers for Photovoltaic Cells. *J. Am. Chem. Soc.* **2009**, *131*, 6050−6051.

(18) Shi, D.; Adinolfi, V.; Comin, R.; Yuan, M.; Alarousu, E.; Buin, A.; Chen, Y.; Hoogland, S.; Rothenberger, A.; Katsiev, K.; et al. Low Trap-State Density and Long Carrier Diffusion in Organolead Trihalide Perovskite Single Crystals. *Science* **2015**, *347*, 519−522.

(19) Saidaminov, M. I.; Abdelhady, A. L.; Murali, B.; Alarousu, E.; Burlakov, V. M.; Peng, W.; Dursun, I.; Wang, L.; He, Y.; Maculan, G.; et al. High-Quality Bulk Hybrid Perovskite Single Crystals within Minutes by Inverse Temperature Crystallization. *Nat. Commun.* **2015**, *6*, No. 7586.

(20) Senocrate, A.; Moudrakovski, I.; Kim, G. Y.; Yang, T.-Y.; Gregori, G.; Grätzel, M.; Maier, J. The Nature of Ion Conduction in Methylammonium Lead Iodide: A Multimethod Approach. *Angew. Chem., Int. Ed.* **2017**, *56*, 7755−7759.

(21) Dong, Q.; Fang, Y.; Shao, Y.; Mulligan, P.; Qiu, J.; Cao, L.; Huang, J. Electron-Hole Diffusion Lengths > 175 Mm in Solution-Grown $CH_3NH_3PbI_3$ Single Crystals. *Science* **2015**, *347*, 967−970.

(22) Maculan, G.; Sheikh, A. D.; Abdelhady, A. L.; Saidaminov, M. I.; Haque, M. A.; Murali, B.; Alarousu, E.; Mohammed, O. F.; Wu, T.; Bakr, O. M. CH3NH3PbCl3 Single Crystals: Inverse Temperature Crystallization and Visible-Blind UV-Photodetector. *J. Phys. Chem. Lett.* **2015**, *6*, 3781−3786.

(23) Chen, Z.; Turedi, B.; Alsalloum, A. Y.; Yang, C.; Zheng, X.; Gereige, I.; AlSaggaf, A.; Mohammed, O. F.; Bakr, O. M. Single-Crystal $MAPbI_3$ Perovskite Solar Cells Exceeding 21% Power Conversion Efficiency. *ACS Energy Lett.* **2019**, *4*, 1258−1259.

(24) Schlipf, J.; Askar, A. M.; Pantle, F.; Wiltshire, B. D.; Sura, A.; Schneider, P.; Huber, L.; Shankar, K.; Müller-Buschbaum, P. Top-Down Approaches Towards Single Crystal Perovskite Solar Cells. *Sci. Rep.* **2018**, *8*, No. 4906.

(25) Chen, Z.; Dong, Q.; Liu, Y.; Bao, C.; Fang, Y.; Lin, Y.; Tang, S.; Wang, Q.; Xiao, X.; Bai, Y.; et al. Thin Single Crystal Perovskite Solar Cells to Harvest Below-Bandgap Light Absorption. *Nat. Commun.* **2017**, *8*, No. 1890.
(26) Hoque, M. N. F.; Islam, N.; Li, Z.; Ren, G.; Zhu, K.; Fan, Z. Ionic and Optical Properties of Methylammonium Lead Iodide Perovskite across the Tetragonal-Cubic Structural Phase Transition. *ChemSusChem* **2016**, *9*, 2692−2698.
(27) Lee, J.-W. W.; Kim, S.-G. G.; Yang, J.-M. M.; Yang, Y.; Park, N.-G. G. Verification and Mitigation of Ion Migration in Perovskite Solar Cells. *APL Mater.* **2019**, *7*, No. 041111.
(28) Eames, C.; Frost, J. M.; Barnes, P. R. F.; O'Regan, B. C.; Walsh, A.; Islam, M. S. Ionic Transport in Hybrid Lead Iodide Perovskite Solar Cells. *Nat. Commun.* **2015**, *6*, No. 8497.
(29) Yang, S.; Chen, S.; Mosconi, E.; Fang, Y.; Xiao, X.; Wang, C.; Zhou, Y.; Yu, Z.; Zhao, J.; Gao, Y.; et al. Stabilizing Halide Perovskite Surfaces for Solar Cell Operation with Wide-Bandgap Lead Oxysalts. *Science* **2019**, *365*, 473−478.
(30) Meloni, S.; Moehl, T.; Tress, W.; Franckeviius, M.; Saliba, M.; Lee, Y. H.; Gao, P.; Nazeeruddin, M. K.; Zakeeruddin, S. M.; Rothlisberger, U.; et al. Ionic Polarization-Induced Current-Voltage Hysteresis in CH3NH3PbX3 Perovskite Solar Cells. *Nat. Commun.* **2016**, *7*, No. 10334.
(31) Zhao, Y. C.; Zhou, W. K.; Zhou, X.; Liu, K. H.; Yu, D. P.; Zhao, Q. Quantification of Light-Enhanced Ionic Transport in Lead Iodide Perovskite Thin Films and Its Solar Cell Applications. *Light Sci. Appl.* **2017**, *6*, No. e16243.
(32) Li, J.; Bouchard, M.; Reiss, P.; Aldakov, D.; Pouget, S.; Demadrille, R.; Aumaitre, C.; Frick, B.; Djurado, D.; Rossi, M.; et al. Activation Energy of Organic Cation Rotation in CH3NH3PbI3 and CD3NH3PbI3: Quasi-Elastic Neutron Scattering Measurements and First-Principles Analysis Including Nuclear Quantum Effects. *J. Phys. Chem. Lett.* **2018**, *9*, 3969−3977.
(33) Yang, T.-Y.; Gregori, G.; Pellet, N.; Grätzel, M.; Maier, J. The Significance of Ion Conduction in a Hybrid Organic-Inorganic Lead-Iodide-Based Perovskite Photosensitizer. *Angew. Chem., Int. Ed.* **2015**, *54*, 7905−7910.
(34) Mosconi, E.; De Angelis, F. Mobile Ions in Organohalide Perovskites: Interplay of Electronic Structure and Dynamics. *ACS Energy Lett.* **2016**, *1*, 182−188.
(35) Saidaminov, M. I.; Adinolfi, V.; Comin, R.; Abdelhady, A. L.; Peng, W.; Dursun, I.; Yuan, M.; Hoogland, S.; Sargent, E. H.; Bakr, O. M. Planar-Integrated Single-Crystalline Perovskite Photodetectors. *Nat. Commun.* **2015**, *6*, No. 9724.
(36) Li, W.-G.; Rao, H.-S.; Chen, B.-X.; Wang, X.-D.; Kuang, D.-B. A Formamidinium−Methylammonium Lead Iodide Perovskite Single Crystal Exhibiting Exceptional Optoelectronic Properties and Long-Term Stability. *J. Mater. Chem. A* **2017**, *5*, 19431−19438.
(37) Albadri, A.; Yadav, P.; Alotaibi, M.; Arora, N.; Alyamani, A.; Albrithen, H.; Dar, M. I.; Zakeeruddin, S. M.; Grätzel, M. Unraveling the Impact of Rubidium Incorporation on the Transport-Recombination Mechanisms in Highly Efficient Perovskite Solar Cells by Small-Perturbation Techniques. *J. Phys. Chem. C* **2017**, *121*, 24903−24908.
(38) Prochowicz, D.; Yadav, P.; Saliba, M.; Saski, M.; Zakeeruddin, S. M.; Lewiński, J.; Grätzel, M. Reduction in the Interfacial Trap Density of Mechanochemically Synthesized $MAPbI_3$. *ACS Appl. Mater. Interfaces* **2017**, *9*, 28418−28425.
(39) Prochowicz, D.; Tavakoli, M. M.; Kalam, A.; Chavan, R. D.; Trivedi, S.; Kumar, M.; Yadav, P. Influence of A-Site Cations on the Open-Circuit Voltage of Efficient Perovskite Solar Cells: A Case of Rubidium and Guanidinium Additives. *J. Mater. Chem. A* **2019**, *7*, 8218−8225.
(40) García-Rodríguez, R.; Ferdani, D.; Pering, S.; Baker, P. J.; Cameron, P. J. Influence of Bromide Content on Iodide Migration in Inverted $MAPb(I_{1-x}Br_x)_3$ Perovskite Solar Cells. *J. Mater. Chem. A* **2019**, *7*, 22604−22614.
(41) Lopez-Varo, P.; Jiménez-Tejada, J. A.; García-Rosell, M.; Ravishankar, S.; Garcia-Belmonte, G.; Bisquert, J.; Almora, O. Device Physics of Hybrid Perovskite Solar Cells: Theory and Experiment. *Adv. Energy Mater.* **2018**, *8*, No. 1702772.
(42) Neukom, M. T.; Schiller, A.; Züfle, S.; Knapp, E.; Ávila, J.; Pérez-del-Rey, D.; Dreessen, C.; Zanoni, K. P. S.; Sessolo, M.; Bolink, H. J.; et al. Consistent Device Simulation Model Describing Perovskite Solar Cells in Steady-State, Transient, and Frequency Domain. *ACS Appl. Mater. Interfaces* **2019**, *11*, 23320−23328.
(43) Moia, D.; Gelmetti, I.; Calado, P.; Fisher, W.; Stringer, M.; Game, O.; Hu, Y.; Docampo, P.; Lidzey, D.; Palomares, E.; et al. Ionic-to-Electronic Current Amplification in Hybrid Perovskite Solar Cells: Ionically Gated Transistor-Interface Circuit Model Explains Hysteresis and Impedance of Mixed Conducting Devices. *Energy Environ. Sci.* **2019**, *12*, 1296−1308.
(44) De Bastiani, M.; Dell'Erba, G.; Gandini, M.; D'Innocenzo, V.; Neutzner, S.; Kandada, A. R. S.; Grancini, G.; Binda, M.; Prato, M.; Ball, J. M.; et al. Ion Migration and the Role of Preconditioning Cycles in the Stabilization of the *J - V* Characteristics of Inverted Hybrid Perovskite Solar Cells. *Adv. Energy Mater.* **2016**, *6*, No. 1501453.
(45) Jacobs, D. A.; Shen, H.; Pfeffer, F.; Peng, J.; White, T. P.; Beck, F. J.; Catchpole, K. R. The Two Faces of Capacitance: New Interpretations for Electrical Impedance Measurements of Perovskite Solar Cells and Their Relation to Hysteresis. *J. Appl. Phys.* **2018**, *124*, No. 225702.
(46) Almora, O.; Zarazua, I.; Mas-Marza, E.; Mora-Sero, I.; Bisquert, J.; Garcia-Belmonte, G. Capacitive Dark Currents, Hysteresis, and Electrode Polarization in Lead Halide Perovskite Solar Cells. *J. Phys. Chem. Lett.* **2015**, *6*, 1645−1652.
(47) Milot, R. L.; Eperon, G. E.; Snaith, H. J.; Johnston, M. B.; Herz, L. M. Temperature-Dependent Charge-Carrier Dynamics in CH3NH3PbI3 Perovskite Thin Films. *Adv. Funct. Mater.* **2015**, *25*, 6218−6227.
(48) Yuan, Y.; Chae, J.; Shao, Y.; Wang, Q.; Xiao, Z.; Centrone, A.; Huang, J. Photovoltaic Switching Mechanism in Lateral Structure Hybrid Perovskite Solar Cells. *Adv. Energy Mater.* **2015**, *5*, No. 1500615.
(49) Delugas, P.; Caddeo, C.; Filippetti, A.; Mattoni, A. Thermally Activated Point Defect Diffusion in Methylammonium Lead Trihalide: Anisotropic and Ultrahigh Mobility of Iodine. *J. Phys. Chem. Lett.* **2016**, *7*, 2356−2361.
(50) Almora, O.; García-Batlle, M.; Garcia-Belmonte, G. Utilization of Temperature-Sweeping Capacitive Techniques to Evaluate Band Gap Defect Densities in Photovoltaic Perovskites. *J. Phys. Chem. Lett.* **2019**, *10*, 3661−3669.
(51) Bube, R. H. Trap Density Determination by Space-Charge-Limited Currents. *J. Appl. Phys.* **1962**, *33*, 1733−1737.
(52) Poglitsch, A.; Weber, D. Dynamic Disorder in Methylammoniumtrihalogenoplumbates (II) Observed by Millimeter-wave Spectroscopy. *J. Chem. Phys.* **1987**, *87*, 6373−6378.
(53) Das, S.; Chaudhuri, S. K.; Bhattacharya, R. N.; Mandal, K. C. Defect Levels in $Cu_2ZnSn(S_xSe_{1-x})_4$ Solar Cells Probed by Current-Mode Deep Level Transient Spectroscopy. *Appl. Phys. Lett.* **2014**, *104*, No. 192106.
(54) Balcioglu, A.; Ahrenkiel, R. K.; Hasoon, F. Deep-Level Impurities in CdTe/CdS Thin-Film Solar Cells. *J. Appl. Phys.* **2000**, *88*, 7175−7178.
(55) Ayres, J. R. Characterization of Trapping States in Polycrystalline silicon Thin Film Transistors by Deep Level Transient Spectroscopy. *J. Appl. Phys.* **1993**, *74*, 1787−1792.

https://dx.doi.org/10.1021/acs.jpcc.9b11343
J. Phys. Chem. C 2020, 124, 3496−3502